



Photoconductivity in self-assembled CuO thin films

Akhil M. Anand¹ · Aruna Raj¹ · Jishad A. Salam¹ · R. Adithya Nath¹ · R. Jayakrishnan¹

Received: 8 September 2023 / Accepted: 12 December 2023 / Published online: 16 February 2024
© The Author(s) 2024

Abstract

Self-assembly is the most promising low-cost and high-throughput methodology for nanofabrication. This paper reports the optimization of a self-assembly process at room temperature for the growth of copper oxide (CuO) based nanostructures over a copper substrate using aqueous potassium hydroxide (KOH) solution as the oxidizing agent. The monoclinic phase of CuO nanostructures grown over the copper substrate was confirmed from the X-ray diffraction (XRD) and micro-Raman analysis. The overall chemical composition of nanostructures was confirmed to be that of CuO from its oxidation state using X-ray photoelectron spectroscopy (XPS). Photodetectors were engineered with the structure Cu/CuO/Ag. The photodetectors exhibited a response to both ultraviolet and visible light illumination. The optimized Cu/CuO/Ag structure exhibits a responsivity of $\sim 1.65 \mu\text{A/W}$, with an ON:OFF ratio of ~ 69 under a bias voltage of 0.01 V. The temporal dependence of photo-response for the optimized photodetector displayed the persistent nature of photoconduction indicating a delay in charge carrier recombination which could potentially be exploited for photovoltaic applications.

Keywords Self-assembly · Copper oxide · Molarity variation · Photovoltaic application

Introduction

Self-assembly is a process observed in nature at different dimensions. During self-assembly, spontaneous ordering of atoms/molecules occurs over a broad length scale ranging from angstrom to centimeters in different dimensions without human intervention which makes the technique industrially relevant for the electronics and optoelectronics industry. Because of its ubiquitous occurrence in natural systems, it favors the bottom-up growth of materials. These features make it one of the most promising, low-cost, high-throughput, and practically scalable methodologies for nanofabrication [1]. Recently, there has been remarkable attention on metal oxide semiconductors (MOS) due to their optical, electrical, and thermal properties that make them unavoidable in technological frontiers like nano-electronics, solar cells, sensors, and photo catalysis. They are highly sensitive and have a very short response time when engineered in the nanoscale [2]. MOS are valence compounds with a high

degree of ionic bonding. Their conduction band minimum (CBM) and valence band maximum (VBM) mainly consist of the metal (M) ns and oxygen (O) 2p orbital, respectively [3]. The interaction between the metal and oxide orbitals results in better electron transport in comparison to hole transport.

Copper oxide is an industrially important material with a wide range of applications in solar energy conversion, gas and biosensor technology, energy storage media, spintronics, optoelectronics, catalysis, biomedicine, batteries, supercapacitors, and high-temperature superconductors [4, 5]. The most common, stable, and non-toxic phases of copper oxides are cupric oxide (CuO) and cuprous oxide (Cu₂O) [6]. The optical band gap of CuO ranges from 1.2 to 1.9 eV while the band gap of Cu₂O ranges from 2.0 to 2.6 eV [6]. Cu₂O has a high absorption coefficient in the visible region and is suitable for applications in solar cells [7]. However, Cu₂O is thermally unstable and turns into CuO with heat treatment, so this latter phase is preferred for applications in solar cells operating under high-temperature conditions [8]. The CuO thin films have a p-type semiconductor property with a narrow optical bandgap and a high absorption coefficient in the visible and near-infrared (NIR) region, making the CuO thin film suitable as an absorber layer for solar cell applications [9]. The surface oxygen adsorption capacity

✉ R. Jayakrishnan
rjk@keralauniversity.ac.in

¹ Photovoltaic Research Laboratory, Department of Physics, University of Kerala, Kariavattom, Thiruvananthapuram 695581, Kerala, India

of CuO is quite high so it can be effectively used for gas-sensing applications [10].

Very few reports on the growth of CuO thin films using wet chemical oxidative mechanisms are available in the literature that focuses on their optoelectronic applications [11]. Most of the works on wet chemistry-grown CuO are concentrated on super-capacitor application, photo-catalysis, antimicrobial applications, etc. [4, 12]. Most of the previous reports on alkaline wet chemical oxidation mechanisms are based on the use of oxidizing agents of a concentration lower than 0.5 M [11]. Aqueous KOH is alkaline in nature and dissociates to form hydroxide ions. Hence, it yields a substitution reaction when water is used as the solvent. Reports on the room temperature growth of CuO on a Cu foil using aqueous KOH are inadequate and this report is a harbinger in this area. In this work, we report on the photoconductivity of self-assembled CuO nano-structured thin films grown over Cu foil and explore its applicability for ultraviolet and visible light photo-detection.

Materials and methods

Synthesis of CuO thin films

All reagents used in this experiment require no further purification as they are of analytical (AR) grade. At first, flexible copper foil (thickness 0.25 mm, 99.98%) is cleaned using 4 M HCL solution for 15 min. After that, the foil is washed with an alkaline cleansing solution and deionized water. Cleaned copper substrates are dried in air at 60 °C for 15 min. Subsequently, 0.1 M solution of potassium hydroxide (KOH, Sigma Aldrich, 99.95%) was prepared in 100 ml distilled water. The treated copper foils were immersed into the KOH solution at room temperature and kept undisturbed for 6 days in a dark room maintained under ambient air conditions. A dark black uniform film appears over the copper foils over a period of time. At the

end of the process, the copper sheets were carefully washed several times with deionized water and dried at 60 °C for 5 h. A schematic representation of thin film formation is shown in Fig. 1. Comparative studies were carried out by changing the molarity of the KOH solution to 0.1 M, 0.5 M, 1 M, 1.5 M, and 2 M with sample codes CuO0.1 M, CuO0.5 M, CuO1 M, CuO1.5 M, and CuO2 M, respectively.

Device engineering

A metal–semiconductor–metal (MSM) structure was developed for photodetector application. Silver (Ag) was used to make metallic contact over CuO surface. Ag, hence, serves as the front electrode. The base copper sheet serves as the back contact for the photodetector device engineered by us. A schematic representation of the Cu-CuO/Ag device structure is shown in Fig. 1b. Current–voltage measurements were taken under dark and visible illumination conditions. For visible light illumination, a halogen source of power density 70 W/m² was used.

Experimental characterizations

X-ray diffraction (XRD) analysis was carried out using Bruker D8 Advance Diffractometer (Cu K α radiation $\lambda = 1.5406 \text{ \AA}$) incorporated with a Lynx Eye position-sensitive detector with a step size of 0.02°. Micro-Raman spectra were recorded using a LabRAM, Horiba with a laser excitation source of wavelength 532 nm. Elemental composition confirmation was carried out using X-ray photoelectron spectroscopy with Thermo Scientific ESCALAB Xi + XPS system with Al-K α radiation (1486.6 eV) as the source of excitation. The surface morphology was recorded using JEOL 6390LA/OXFORD XMX N. Diffused reflectance spectroscopy (DRS) studies were conducted using a JASCO V-750 double-beam spectrophotometer with a photomultiplier tube detector. Current–voltage characteristics as well

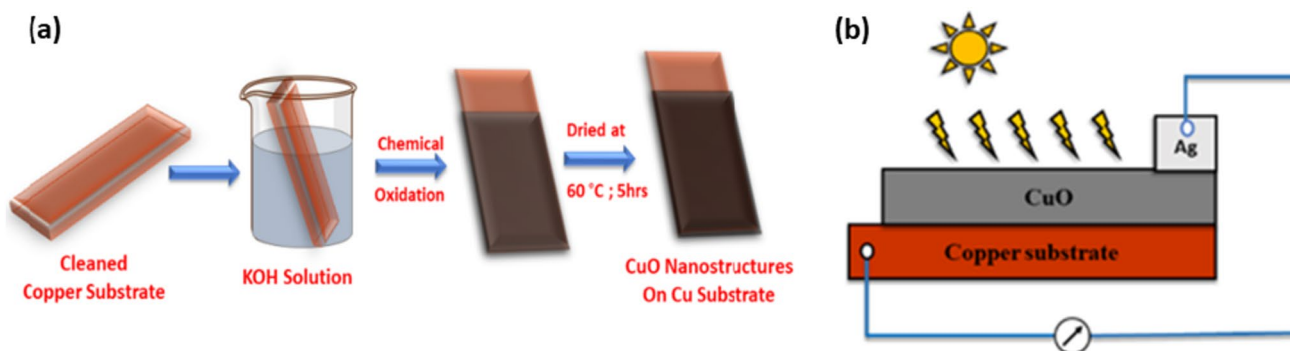


Fig. 1 Schematic image of **a** CuO nanostructure self-assembly and **b** photodetector

as photodetector properties were studied using a Keysight B2910BL source measuring unit.

Results and discussions

Figure 2 describes the observed relationship between thin film thickness at the end of 6 days and the KOH concentration used. It is observed that the thickness of the deposited CuO thin films has a direct relationship with the KOH concentration when the number of days of self-assembly was kept fixed. The measurements show the thickness of the films is in the range of ~1.3–2.1 μm . Beyond the 6-day growth period, we observed that the films were beginning to peel off from the substrate.

XRD patterns of CuO thin films grown using different KOH molarity conditions are shown in Fig. 3. For all of the five samples, XRD peaks were observed at 2θ values of 32.56° , 35.58° , 38.76° , 48.95° , 53.39° , 58.26° , 66.46° , 68.05° and 75.20° which could be indexed to the (110), (002), (111), (20 $\bar{2}$), (020), (202), (31 $\bar{1}$), (220), and (22 $\bar{2}$) planes respectively of the monoclinic CuO (ICCD-96-101-1195).

The peaks at 2θ values of 43.40° and 50.56° could be attributed to (111) and (200) planes of cubic structured Cu (ICCD-96-901-2955). The calculated unit cell parameters are tabulated in Table 1. We observed that the intensity of Cu peaks decreases as the concentration of KOH increases which could be reasoned to the increase in thickness of the samples corresponding to the increase in the KOH concentration. For CuO1.5 M an additional peak was observed at 36.56° and for CuO2 M samples, two additional peaks at 36.56° and 42.42° were observed which corresponds to

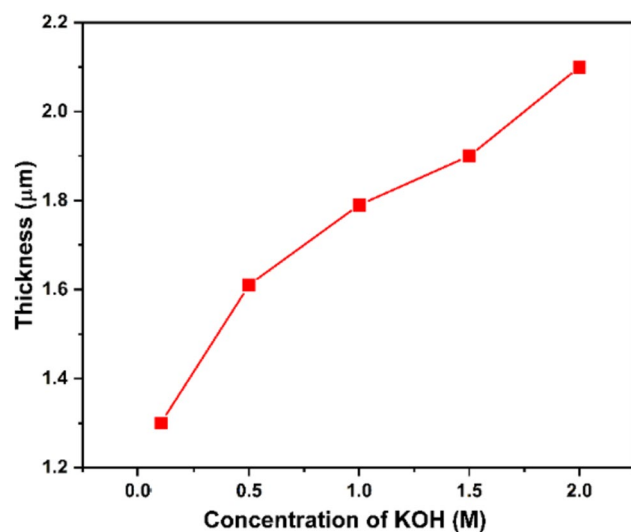


Fig. 2 Variation of CuO thin film thickness with KOH concentration

the (111) and (020) planes respectively of cubic Cu_2O (96-101-0942). This observation could be recognized as the deposition of Cu_2O on the copper foil due to an incomplete reaction at the film–foil interface [12]. Nuengruethai et al. reported that Cu_2O impurities occur in facile deposited CuO nanostructures as the deposition time increases [12]. From XRD analysis, it is clear that when the molarity of the KOH solution is increased beyond 1 M additional Cu_2O impurities occur. Among the three samples CuO0.1 M, CuO0.5 M, and CuO1 M where no Cu_2O impurities were identified the CuO1 M samples show relatively higher XRD intensity for all CuO peaks. Hence this sample was identified to be the optimum in terms of its crystallization. Figure S1 (supplementary) shows the magnified peak images of 2θ values 36.56° and 42.42° .

The Scherrer equation was used to determine the average crystallite size (D) of the CuO thin films [13]:

$$D = \frac{K\lambda}{\beta\cos(\theta)}, \quad (1)$$

where K is the Scherrer constant ($K=0.9$), which is affected by the size distribution and crystallite form, $\lambda=1.5418 \text{ \AA}$ is the X-ray wavelength, θ is the Bragg angle, and β is the full width at half maximum (FWHM) of the plane.

Using the average crystallite size (D), the crystallites number (N) was determined using the relation [6]:

$$N = \frac{1}{D^3}. \quad (2)$$

Micro-strain (ϵ) in the samples were evaluated using the relation (3) which is a prominent source for the XRD peak broadening [14]:

$$\epsilon = \frac{\beta\cot(\theta)}{4}. \quad (3)$$

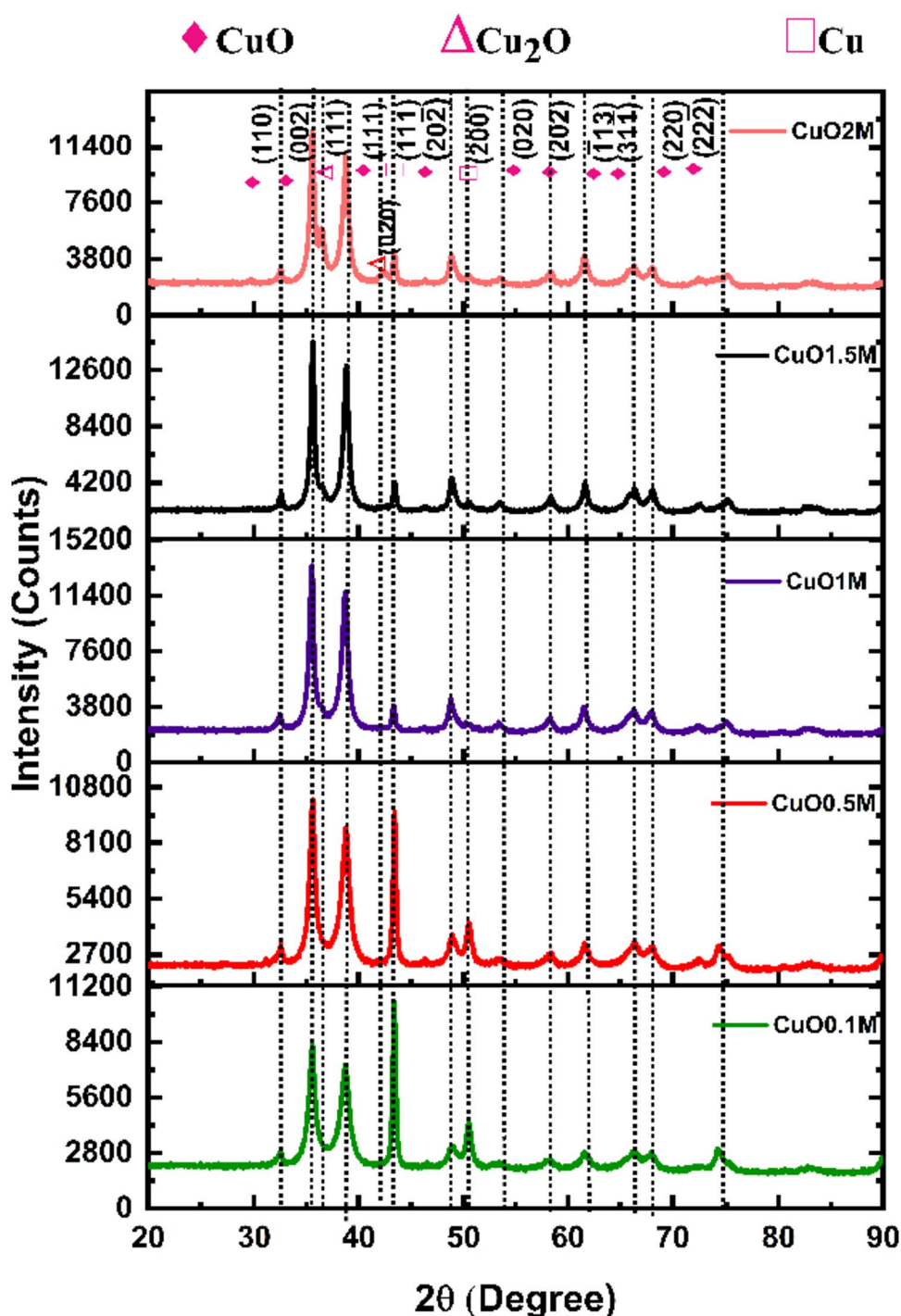
Dislocation density (δ), which is defined as the number of dislocation lines per unit volume through the film surface was evaluated using relation (4) [6]:

$$\delta = \frac{1}{D^2}. \quad (4)$$

Table 1 summarizes the results of the calculations conducted for evaluating average crystallite size (D), micro-strain (ϵ), and dislocation density (δ) for the grown thin film samples.

Figure 4 shows the high-resolution TEM image and selected area electron diffraction (SAED) image of the CuO1 M sample. From Fig. 4a, b, it is evident that the deposited CuO material is nanostructured which exhibits a shape identical to that of nanopetals. Figure 4c shows the lattice under the magnified scale of 2 nm, from which the diffraction line inter-planar distance is measured as 0.25 nm and

Fig. 3 XRD patterns of CuO0.1 M, CuO0.5 M, CuO1 M, CuO1.5 M and CuO2 M samples



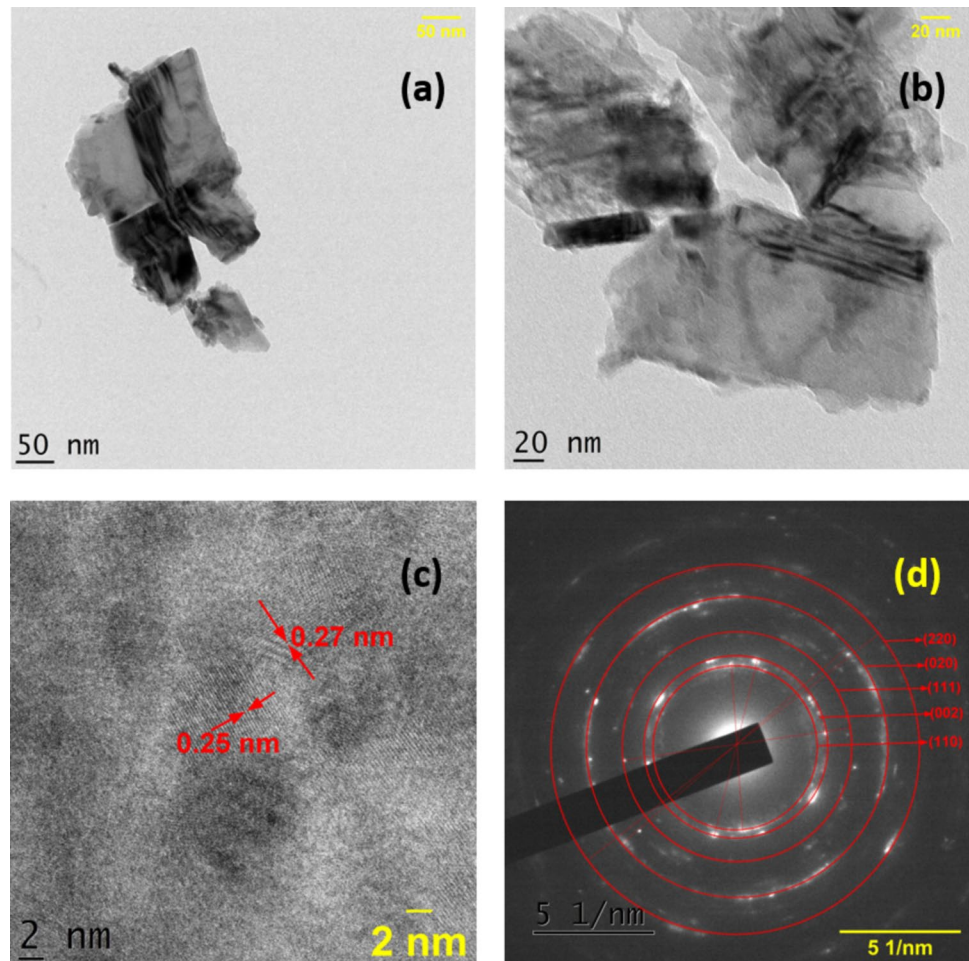
0.27 nm which corresponds to the inter-planar spacing of (110) and (002) planes for monoclinic CuO, respectively. Figure 4d, which represents the selected-area diffraction pattern of the sample, is useful for determining the type of structural ordering in the material. The presence of concentric ring-like structures with diffuse spots indicates that the grown material is polycrystalline in nature. The planes (110), (002), (111), (020), and (220) corresponding to the monoclinic phase of CuO could be indexed from the SAED

pattern. The results of the HR-TEM analysis complement the XRD analysis in identifying the crystal structure of the grown CuO films.

The Raman spectra were used to analyze the nanoparticles' structural characteristics. There are 12 vibrational modes at the zone center of CuO, including three acoustic modes ($A_u + 2B_u$), six infrared-active modes ($3A_u + 3B_u$), and three Raman-active modes ($A_g + 2B_g$) [15]. The Raman spectra of the freshly made CuO nanostructures

Table 1 Summary of calculated values of unit cell parameters, crystallite size, strain, dislocation density, and crystallite number for the CuO thin film samples

Sample code	Crystal unit cell parameters			Crystallite size D (nm)	Strain $\times 10^{-3}$, ϵ	Dislocation density, $\delta \times 10^{15}$ (lines/m ²)	Crystallites number, $N \times 10^{23}$ (m ⁻³)
	a (Å)	b (Å)	c (Å)				
CuO0.1 M	4.601	3.428	5.041	13	8.72	5.9	4.5
CuO0.5 M	4.608	3.425	5.041	14	8.03	5.1	3.6
CuO1 M	4.628	3.431	5.053	17	6.55	3.4	2.0
CuO1.5 M	4.595	3.423	5.040	21	5.30	2.2	1.0
CuO2 M	4.611	3.423	5.047	22	5.17	2.0	0.9

Fig. 4 **a, b** High resolution-TEM images **c** lattice under 2 nm magnification scale and **d** selected area electron diffraction (SAED) images of CuO1 M sample

are displayed in Fig. 5. Three Raman peaks can be recognized at 280, 330, and 620 cm^{-1} , respectively. The Raman peaks are wider and downshifted when compared to the Raman vibrational spectra of a CuO single crystal [16]. The peak at 273 cm^{-1} belongs to the A_g mode, while the peaks at 321 and 606 cm^{-1} belongs to the B_g modes [15]. The quantum confinement effect of CuO nanorods is primarily responsible for the broadenings and downshifts of the Raman peaks [15].

XPS is used to characterize changes in the chemical environment of an element in a structure because of the short inelastic mean free path (IMFP) and sensitivity of the photoelectrons to their chemical surroundings [17]. Figure 6 shows the XPS results obtained from the optimal sample CuO1 M. The survey spectrum in Fig. 6a reveals the presence of the elements copper, oxygen, and carbon. Figure 6b, c shows the XPS spectra of Cu2p and O1s. In Fig. 6b two Cu peaks at 933.9 and 953.9 eV, corresponding to the Cu2p_{3/2}

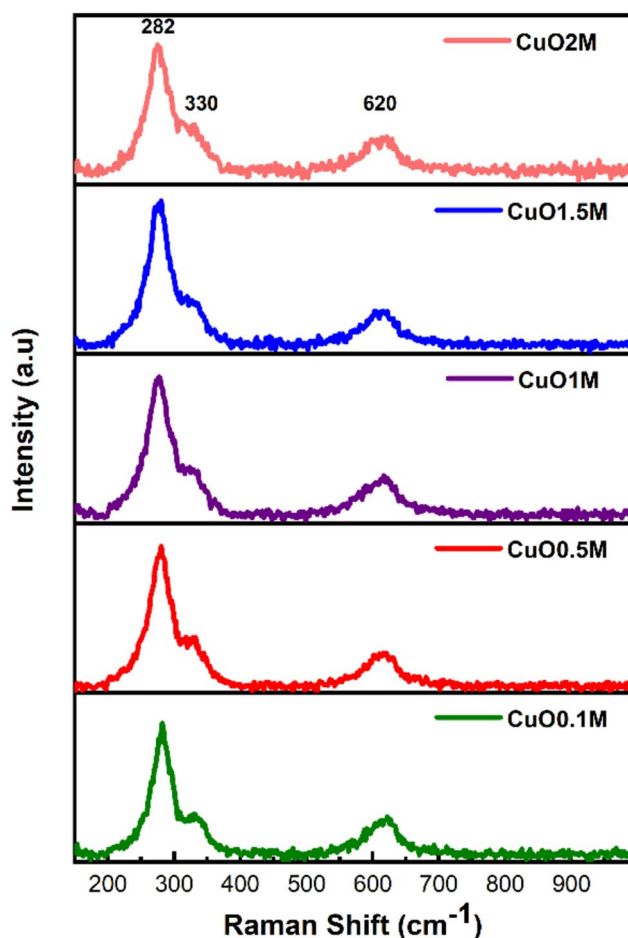


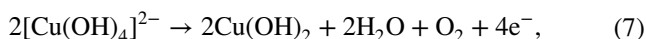
Fig. 5 Raman spectra of CuO samples

and Cu $2p_{1/2}$ peaks of Cu^{2+} respectively confirm the existence of CuO. The peaks at 941.72 eV and 944.20 eV are satellite peaks of $\text{Cu}2p_{3/2}$. The peak at 962.51 eV corresponds to the satellite peak of $\text{Cu}2p_{1/2}$. The O1s spectrum as shown in Fig. 6c consists of two oxygen contributions identified as O^{2-} in CuO at 529.7 eV and oxygen adsorbed onto the surface of CuO particles at 531.2 eV [18]. XPS analysis confirms the chemical composition of the films to be CuO and complements the structural identification of the monoclinic CuO phase obtained from XRD and Raman analysis.

The surface pattern of CuO nano structure was studied using scanning electron microscopy (SEM). Figure 7 shows the SEM image of the optimized CuO1 M sample at different magnifications. SEM image confirms the formation of 2D self-assembled nanostructured fibrous surface morphology over Cu foil. The surface image of the CuO grown on the copper foil as shown in Fig. 7a, shows the bundled nature of the fibrous structures whereas the image shown in Fig. 7b reveals that needle like structures with an average thickness ~ 130 nm are stacked homogeneously over the surface. There appears to be a globular pattern on the large scale

distinct from each other composed of these needle-like structures forming a structure resembling the petals of a flower.

We propose the following mechanism for the growth of CuO thin films in our process: clean and new copper foils are separately submerged in 100 mL of KOH at different concentrations during the first stage of the synthesis. Copper foil, being the source of copper begins to degrade by releasing Cu^{2+} ions into the solutions, leaving behind electrons. The Cu^{2+} ions get continually discharged into the solutions at a very quick oxidation rate [19]. Since Cu^{2+} and O^{2-} are the most stable oxidation states, the released ions interact with hydroxyl ions and result in the formation of $\text{Cu}(\text{OH})_2$ which precipitates on top of the copper foils, which then becomes CuO (solid films) after 5 h of dehydration at 60 °C. High OH^- concentrations could also lead to the formation of $[\text{Cu}(\text{OH})_4]^{2-}$ complex ions which is precipitated as $\text{Cu}(\text{OH})_2$ and then are broken down into CuO (solid films) through the dehydration process [12]. Anisotropic particles are formed at this stage as a result of the concentration of OH^- ions having a net impact on the nucleation and growth processes, such that the number of nuclei, growth units, and the pace at which certain crystalline faces grow are balanced [20, 21]. The above mechanism can be illustrated using Eqs. (5)–(8).



The optical properties of the samples were characterized by UV–visible diffused reflectance spectroscopy (DRS). Figure 8a shows the DRS spectra of different CuO samples. The Kubelka–Munk model is used to evaluate the optical band gap energy of the samples. The value of $F(R)$ is calculated using the equation [12]:

$$F(R) = \frac{(1 - R)^2}{2R}, \quad (9)$$

where $F(R)$ is the Kubelka–Munk function and R is the reflectance. Figure 8b shows the values of $(F(R)h\nu)^2$ vs $h\nu$. For obtaining the band gap energy, the straight line part of the graph is stretched out to intercept the $h\nu$ axis. The intercept value corresponds to the band gap energy [10]. The calculated band gap energies of CuO0.1 M, CuO0.5 M, and CuO1 M are 1.48, 1.47 and 1.45 eV respectively, whereas the band gap of CuO1.5 M and CuO2 M are 1.6 and 1.61 eV. These large band gaps ≥ 1.6 eV can be attributed to the presence of Cu_2O impurities in the samples. Generally, Cu_2O has greater band gap value than CuO [18].

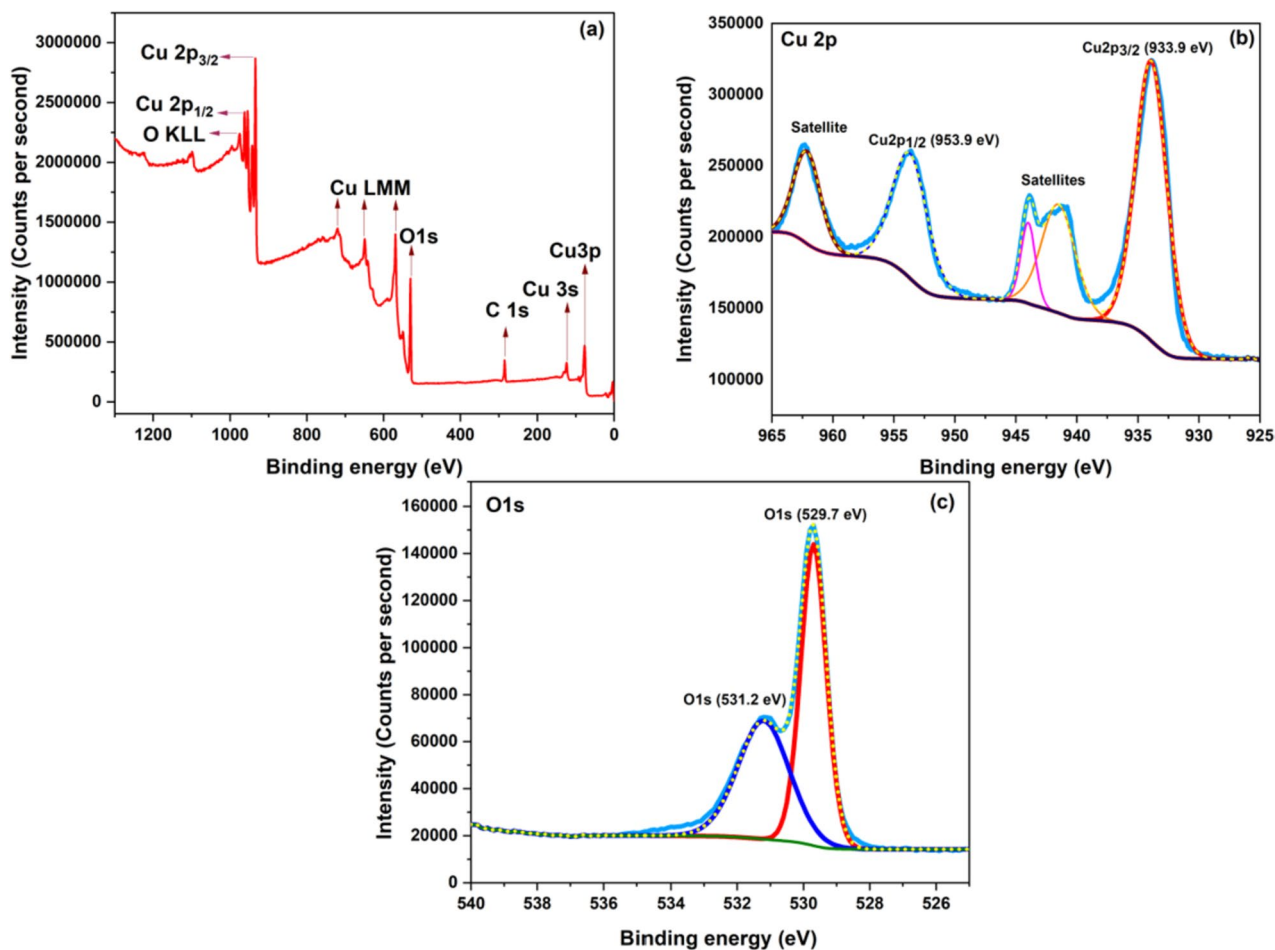


Fig. 6 XPS of CuO1 M sample a survey spectrum b Cu_{2p_{3/2}} spectra and c O1s spectra

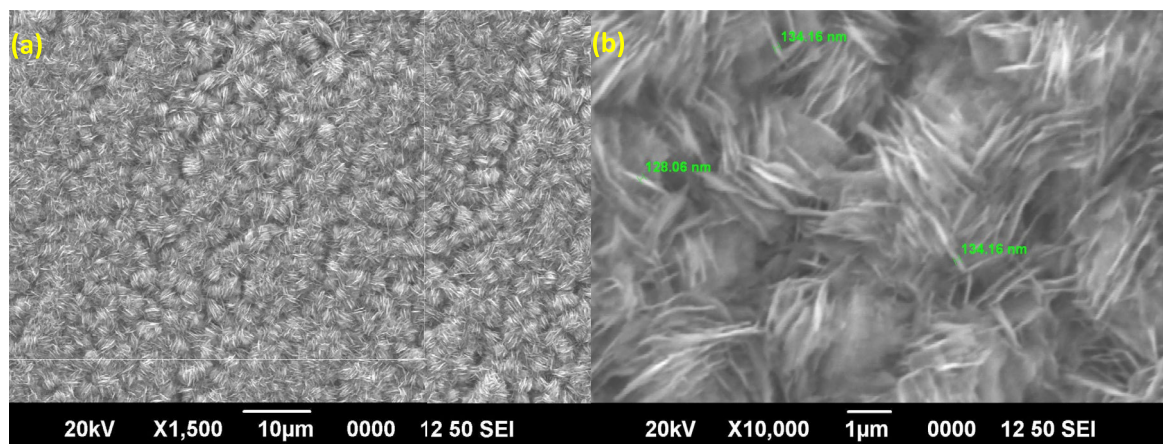


Fig. 7 SEM images of the CuO1 M sample at a scale of a 10 μm and b 1 μm

Figure 9a–e illustrates current voltage characteristics of Ag/CuO/Cu device structure at room temperature in the voltage range – 1 V to +1 V under dark, UV illumination, and

halogen illumination conditions. Current–voltage characteristics of the device show typical diode behavior with lower

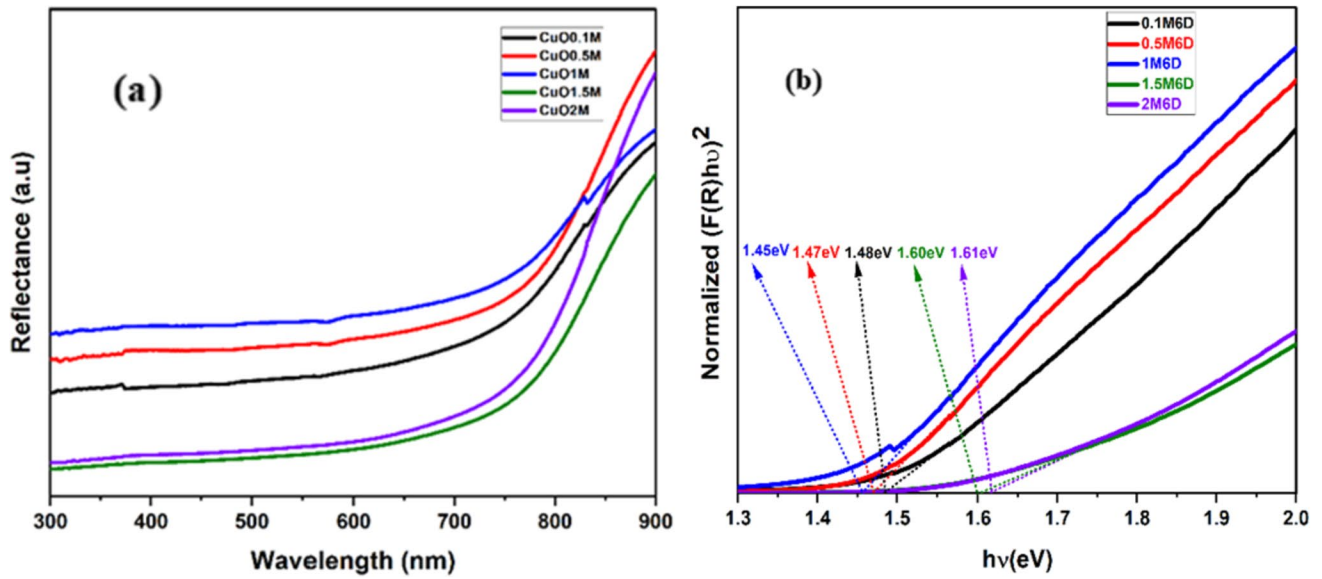


Fig. 8 Graphical representation of reflectance and $F(R)$ spectra for prepared CuO samples (a) reflectance versus wavelength and (b) $F(R)$ versus energy

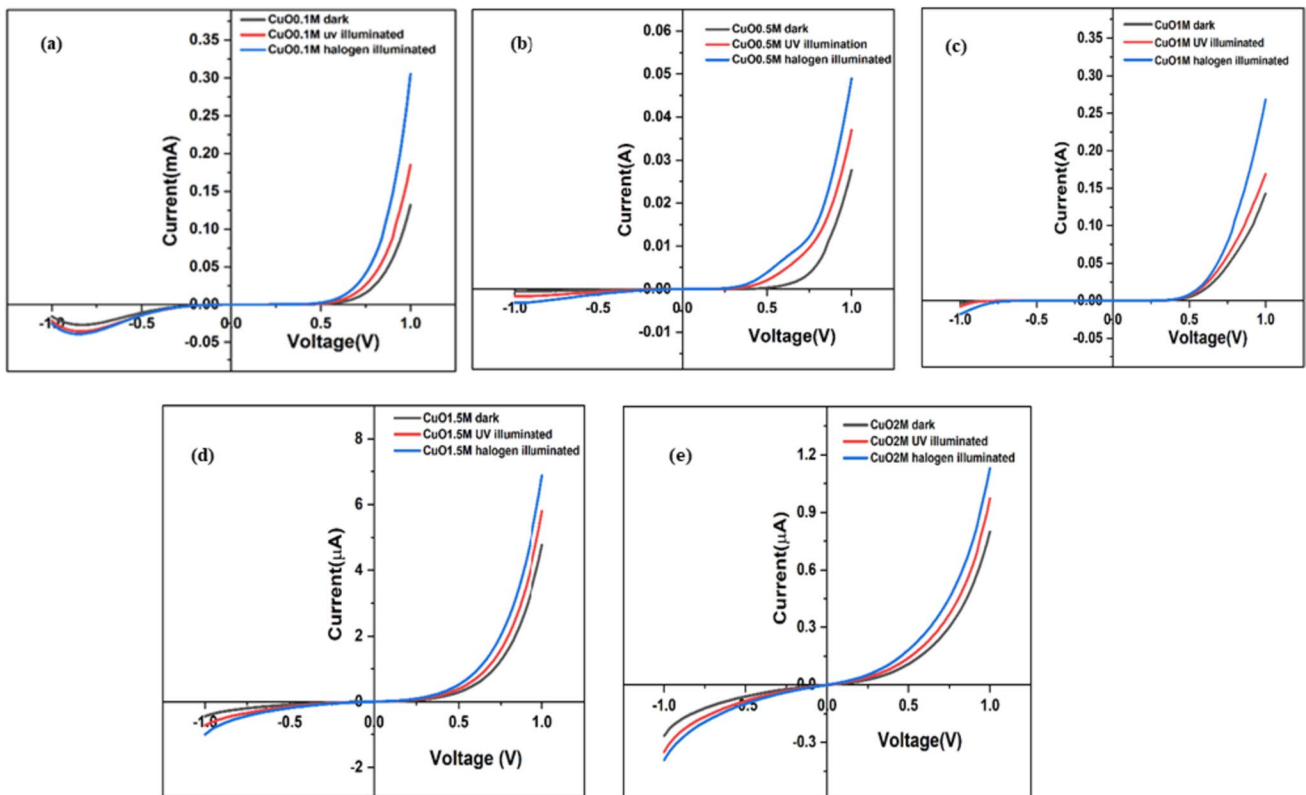


Fig. 9 I - V characteristics under dark, UV and halogen illuminated conditions for samples **a** CuO0.1 M **b** CuO0.5 M **c** CuO1 M **d** CuO 1.5 M and **e** CuO2 M

reverse current and higher forward current which highlights the rectification ratio of the diode.

Under halogen and UV illumination, incident photons are absorbed, and electron-hole pairs are generated which

results in the generation of photocurrent. The photosensitivity, defined as $\left(\frac{I_{\text{illu}} - I_{\text{dark}}}{I_{\text{dark}}}\right) \times 100$ [22], and rectification ratios of all samples are summarized in Table 2. Among all samples, CuO1 M shows a good rectification ratio and photosensitivity.

As per the thermionic emission model current across the Schottky barrier can be expressed as [23]:

$$I = I_0 \left(\exp\left(\frac{qV}{nK_B T}\right) - 1 \right), \quad (10)$$

where K is the Boltzman constant, n is the ideality factor, T is the temperature in kelvin, R is the series resistance, q is the electronic charge, I_0 is the reverse saturation current where I_0 is defined as [24]:

$$I_0 = AA^* T^2 \exp\left(\frac{-q\Phi}{K_B T}\right), \quad (11)$$

Here A and A^* is the effective area of the diode and Richardson constant ($979.36 \text{ Acm}^{-2} \text{ K}^{-2}$ for CuO) [25] respectively and Φ is the zero bias barrier height.

The series resistance of the Schottky junction was determined using the Cheung-Cheung model [26] in the nonlinear part of the high current region. The following relation is used to calculate the series resistance

$$\frac{dV}{d \ln I} = IR_s + n \left(\frac{K_B T}{q} \right), \quad (12)$$

$$H(I) = V - n \left(\frac{K_B T}{q} \right) \ln \left(\frac{I}{AA^* T^2} \right), \quad (13)$$

$$H(I) = IR_s + n\Phi. \quad (14)$$

From the Eq. (12), R_s is calculated from the slope of $dV/d(\ln I)$ vs I curve and Y intercept gives the value of n . Series resistance can also be calculated from the slope of $H(I)$ vs I curve. By knowing the value of n , y intercept of $H(I)$ vs I graph determines the zero bias potential barrier Φ [26]. The series resistance, ideality factor and zero bias potential barrier was calculated for all the samples under dark,

UV illumination and halogen illumination and are tabulated in Table 3. For all samples, there is no much difference in series resistance calculated from Eqs. (12) and (14). All the fabricated junctions show decrease in series resistance upon UV and halogen illumination due to the generation of photo carriers followed by photon irradiation. The devices exhibit relatively better to photo response to halogen light illumination compared to UV light illumination.

The non-linear behavior of current–voltage characteristics can be explained using the variation in diode series resistance [23]. Series resistance of CuO1 M is 1.30Ω in dark condition, which is the lowest resistance value obtained, and results in high rectification ratio and good diode quality. Series resistances of CuO1.5 M and CuO2 M are $\sim 5830 \Omega$ and $\sim 5972 \Omega$ respectively. This high resistance value causes nonlinear bending of forward current in the current voltage characteristics and low rectification ratio [23].

The variation in ideality factor for Ag/CuO/Cu junctions from ideal one can be attributed to the contribution of interface surface defects and series resistance [26]. Even though the series resistances is small for CuO1 M and CuO0.5 M, these samples show ideality factors 4.07 and 4.02, respectively which is greater than ideal diode factor. In this case, surface defects may play the role as the series resistance is negligible. The interface surface defects and series resistance in tandem contribute to large n values (6.61 and 10.16) for CuO1.5 M and CuO2 M samples. The obtained n values are comparable with reported values [23, 27]. The zero bias potential barrier height Φ decreases with increase in the KOH molarity initially and subsequently it increases. For CuO0.1 M, CuO0.5 M, CuO1 M, CuO0.5 M and CuO2 M, the barrier heights are 0.78, 0.60, 0.53, 0.74, and 0.74 eV, respectively.

For photo detector studies, Ag/CuO/Cu structure is used as the active device. Since the photosensitivity of CuO samples towards halogen source is higher than UV source, visible light detection is studied here. The working mechanism of fabricated photodetectors could be explained as shown in Fig. 10.

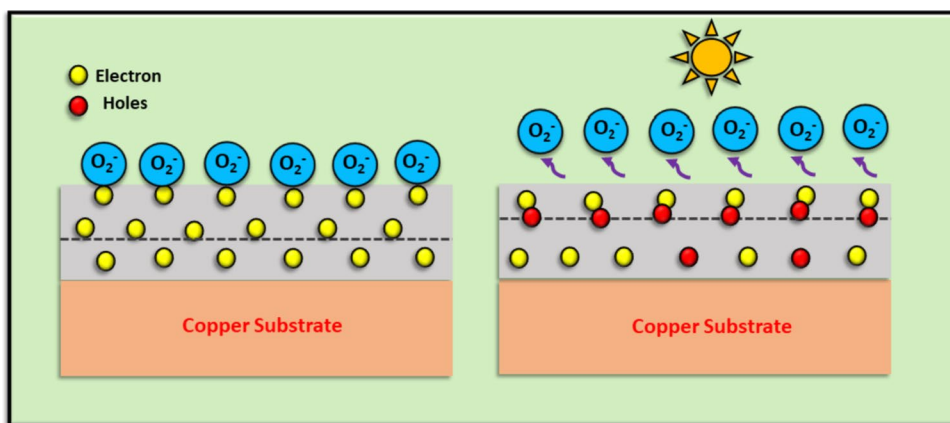
The working of the photodetector is demonstrated under dark and halogen-illuminated conditions at a biasing voltage of 10 mV. In the dark condition, oxygen molecules are adsorbed

Table 2 Photosensitivity and rectification ratio values of the device structures

Sample code	Photo sensitivity (%)		Rectification ratio		
	UV illumination	Halogen illumination	Dark	UV illumination	Halogen illumination
CuO0.1 M	40	131	9	9	12
CuO0.5 M	33	76	53	23	15
CuO1 M	19	88	72	28	17
CuO1.5 M	21	44	11	8	7
CuO2 M	21	41	3	3	3

Table 3 Electrical parameters obtained for all CuO samples

Samples	Condition	Ideality factor (n)	Series resistance (Ω)		Zero bias barrier height, Φ (eV)
			($dV/d\ln I$) vs I	$H(I)$ vs I	
CuO0.1 M	Dark	3.48	436.00	511.86	0.78
	UV illuminated	4.12	260.69	253.08	0.73
	Halogen illuminated	4.22	120.23	117.60	0.72
CuO0.5 M	Dark	4.02	2.54	2.56	0.60
	UV illuminated	5.38	1.91	1.87	0.54
	Halogen illuminated	4.74	1.71	1.72	0.55
CuO1 M	Dark	4.07	1.30	1.38	0.53
	UV illuminated	3.15	1.48	1.55	0.56
	Halogen illuminated	3.82	0.66	0.68	0.53
CuO1.5 M	Dark	6.61	5830.80	5859.36	0.74
	UV illuminated	6.90	4290.44	4159.68	0.73
	Halogen illuminated	7.29	3878.58	3855.69	0.71
CuO2 M	Dark	10.16	5972.47	5908.18	0.74
	UV illuminated	10.21	5011.65	5281.30	0.77
	Halogen illuminated	11.50	4485.57	4624.92	0.68

Fig. 10 Working mechanism of CuO photodetector

to the exposed surface of CuO by capturing electrons from the conduction band.



Adsorbed oxygen creates electron trap sites on the CuO surface. These trapped electron sites owe the formation of a wider less conductive depletion region. When the photodetector is illuminated with a halogen source, electron–hole pairs are generated. Photo-generated holes migrate from the valence band to the surface-trapped oxygen sites to recombine with $\text{O}_2^-(\text{ad})$, thereby discharging O_2 gas into the air and electrons into the conduction band.



This process increases the electron lifetime and successively increases the photocurrent. The oxygen ions are once

more adsorbed to the CuO surface when the light is turned off and the current value drops as a result [14, 28].

Figure 11 shows the switching photo response of fabricated Ag/CuO/Cu photodetectors. The photocurrent time response of the CuO photodetectors was measured at 0.01 V bias under a halogen source on/off lighting with an on/off interval of 10 s. The intensity of the halogen light source was fixed at 70 W/m². The “rise time” is defined as the time required for the photocurrent to increase from its minimum value to 63% of its maximum value and the “decay time” is the time taken for the photocurrent to drop from its maximum magnitude to 37% of its maximum value [29]. The rise and decay times of the device structures are tabulated in Table 4. The responsivity, R is another important term which is the ratio of photocurrent to incident illumination power [30]. The responsivity was calculated using the formula [30]:

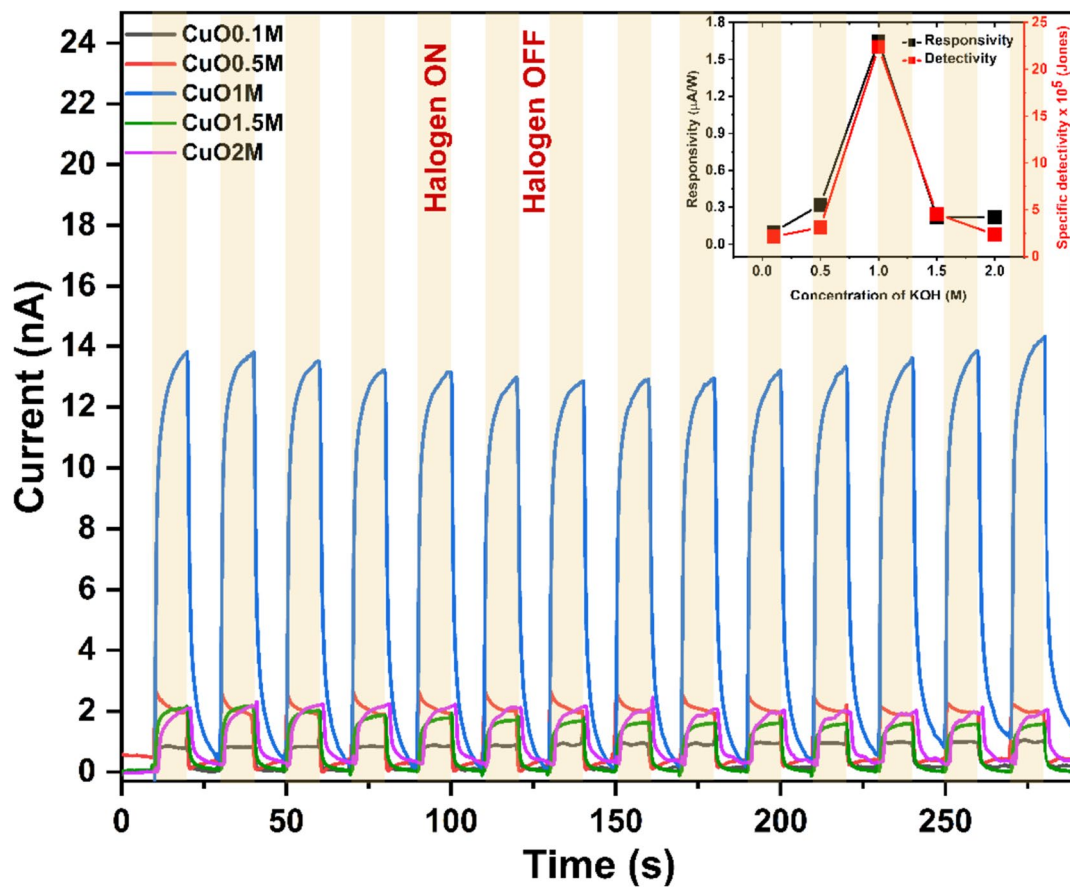


Fig. 11 Switching photo-response (current vs. time) of CuO0.1 M, CuO0.5 M, CuO1 M, CuO1.5 M, and CuO2 M photodetectors

Table 4 Photodetector parameters of all Cu/CuO/Ag detectors

Samples	T_{rise} (s)	T_{decay} (s)	Responsivity ($\mu\text{A/W}$)	ON–OFF ratio	Specific detectivity $\times 10^5$ (Jones)
CuO0.1 M	0.56	0.66	0.10	10.50	2.13
CuO0.5 M	0.56	0.57	0.32	7.60	3.10
CuO1 M	0.57	0.86	1.65	69.40	22.40
CuO1.5 M	0.95	0.65	0.22	22.00	4.55
CuO2 M	0.62	1.13	0.22	6.54	2.35

$$R = \frac{I}{AE}, \tag{17}$$

where R is the responsivity, I is the measured photocurrent, A is the photodetector device's active area, and E is the light source's irradiance intensity, which is measured by a conventional light power meter. Among the five CuO detectors, CuO1 M shows the best responsivity value which is 1.65 $\mu\text{A/W}$. Specific detectability (D^*) which is a figure of merit

for the device determines the weakest detectability of the optical signal and was calculated using the equation [31]:

$$D^* = R \left(\frac{S}{2eI_{dark}} \right)^{\frac{1}{2}}, \tag{18}$$

where R , is the responsivity, S is the effective illumination area, e is the charge of the electron, and I_{dark} is the dark current.

The ON–OFF ratio is defined as the ratio of photocurrent to dark current (I_p/I_d) [29]. All calculated photodetector parameters are tabulated in Table 4.

The current–voltage characteristics reveal that the value of the ideality factor increases with halogen and UV illumination for all photodetectors except CuO1 M. This may be because, under dark conditions, the oxygen molecules that were adsorbed to the surface-trapped sites remain inactive. During illumination, adsorbed oxygen molecules get desorbed and the trapped sites become active for charge carrier trapping. For CuO1 M, the density of defect and trapped sites are less which increases the carrier recombination and thereby decreases the ideality factor. This is supported by the lowered diode series resistance for this device structure. This gives excellent parameters as required for a good photodetector. The inset of Fig. 11 shows the variation of responsivity and specific detectivity with KOH concentration.

Figure 12 represents the transient photo response curve for three of the samples. From Fig. 12, it is evident that the

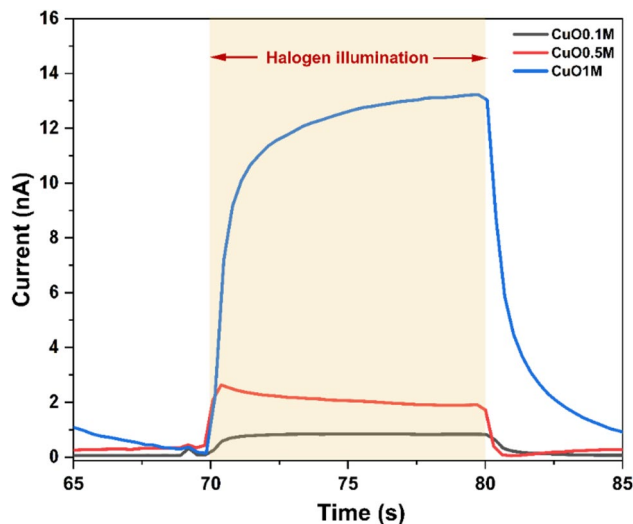


Fig. 12 Time-dependent photo-response (current vs. time) of CuO0.1 M, CuO0.5 M, and CuO1 M photodetectors

photocurrent saturates much faster for the sample CuO0.5 M samples within the illumination pulse period relative to its counterparts. The flat nature of the response indicates that no further charge carriers are being generated as a result of the illuminated condition. On the other hand, for sample CuO0.1 M, the presence of a trap state is evident from the two-level transient response curve. The photocurrent reaches a maximum when illuminated and then decays gradually even when the illumination is maintained and then abruptly decays when illumination is switched off. This temporal dependence indicates that trap states may be activated after the initial rise in photocurrent, and subsequently, the rapid depletion of charge carriers occurs which leads to the abrupt decrease in photocurrent.

For CuO1 M, the rise and decay of photocurrent exhibit the persistent photoconductivity nature associated with deep defect levels [32]. These results indicate that the carrier lifetime is extended in sample CuO1 M relative to all of the other samples prepared by us. The improved photo-response is a manifestation of the improved carrier dynamics which makes it the optimized sample among the set of samples engineered in this work. The persistent nature of photoconduction indicates that the charge carriers are separated as electron–hole pairs for a longer duration of time preventing their recombination. Hence, use of the appropriate electron/hole transport layers could provide an opportunity to extract the carriers for photovoltaic application.

Table 5 summarizes how the electrical parameters of the device were optimized by us compared to other similar photodetectors reported in the literature. Relative to previous reports our device shows substantial responsivity and detectivity under the application of very low bias voltage which is very encouraging. All of the previous works are based on advanced material growth techniques involving expensive processing equipment and rigorous growth conditions [33–39].

Table 5 Summary of photo-response parameters of previously reported CuO-based visible photodetectors

Device structure	Bias voltage	Responsivity	Detectivity	References
FTO/CuO/FTO	0.5 V	60 $\mu\text{A/W}$	1.90×10^8 Jones	[33]
Ag/CuO/Ag	5 V	4085 A/W	3.81×10^{13} Jones	[34]
Au-Cu/CuO/Cu-Au	5 V	200 A/W	6.38×10^{11} Jones	[35]
Ag/CuO/Ag(Blue light)	5 V	0.33 mA/W	2.03×10^8 Jones	[36]
Ag/CuO/Ag(Red light)	5 V	0.59 mA/W	4.60×10^8 Jones	[36]
Cu/CuO/Cu	20 V	2.6 mA/W	2.00×10^9 Jones	[37]
Au/CuO/Au	20 V	0.17 A/W	1.38×10^{11} Jones	[38]
Pd/CuO-Cu ₂ O/Pd	1 V	1105 A/W	1.99×10^{13} Jones	[39]
Pd/CuO/Pd	1 V	689 A/W	1.24×10^{13} Jones	[39]
Cu/CuO/Ag	0.01 V	1.65 $\mu\text{A/W}$	22.4×10^5 Jones	This work

Conclusions

Room temperature self-assembly of CuO thin films on copper foils using a facile solution-immersion method using KOH as the oxidizing agent is achieved in this work. Phase pure CuO thin films with monoclinic structure could be grown on copper foil. Raman and XPS analysis further confirmed the formation of CuO and complimented the XRD results in identifying that the CuO 1 M thin films were the optimally crystallized sample. Our work shows that use of higher KOH concentration results in the formation of Cu₂O impurity phases. This may be due to the decrease in oxidation rate at higher KOH concentrations. Beyond 6 days of wet oxidation, the films tend to peel off from the foil and sediment in the bath which limits the thickness of the CuO films that can be grown by our present process. To study the photo response of the grown CuO thin films, photodetectors were fabricated with the structure Cu/CuO/Ag. The device structure exhibited photo-response to both UV and visible light radiation. Temporal dependence of the photo-response of each device structure to the same illumination pulse showed that the sensitivity mechanism was different for the CuO 0.5 M and CuO 0.1 M samples relative to their counterparts. The current–voltage characteristics revealed the effect of series resistance and ideality factor on the photo-detecting mechanism of the engineered devices. Series resistance plays an indispensable role in the photo-detecting ability of the manufactured devices. Devices with low series resistance and ideality factor have the best photo-detecting properties. The optimized photodetector device structure Cu/CuO/Ag grown at 1 M KOH concentration is found to have a low series resistance of ~ 1.3 Ω and a high ON–OFF ratio of 69.4. The photodetector structure developed by us exhibits a responsivity of ~ 1.65 μA/W and detectivity of 22×10^5 Jones under a bias of 0.01 V. These characteristics for a wet chemically grown photodetector are competitive relative to other CuO-based photodetectors engineered using contemporary techniques.

Acknowledgements AA would like to thank University of Kerala for providing research grants under the UJRF/USRF scheme. RJK would like to thank the University of Kerala for funding of the works vide order No. 1599/2021/UOK dated 22.03.2021 and AD AV order no. 3092/2021/UOK dated 28.06.2021.

Author contributions AMA: conceptualization, investigation, data curation, methodology, software, visualization, and writing—original draft, AR: formal analysis and software, JAS: formal analysis and software, RAN: formal analysis and software, RJ: conceptualization, data curation, methodology, resources, supervision, writing—editing and review.

Data availability Data will be made available on request.

Declarations

Conflict of interest The authors declare that they have no known competing financial interests or personal relationships that could have appeared to influence the work reported in this paper.

Open Access This article is licensed under a Creative Commons Attribution 4.0 International License, which permits use, sharing, adaptation, distribution and reproduction in any medium or format, as long as you give appropriate credit to the original author(s) and the source, provide a link to the Creative Commons licence, and indicate if changes were made. The images or other third party material in this article are included in the article's Creative Commons licence, unless indicated otherwise in a credit line to the material. If material is not included in the article's Creative Commons licence and your intended use is not permitted by statutory regulation or exceeds the permitted use, you will need to obtain permission directly from the copyright holder. To view a copy of this licence, visit <http://creativecommons.org/licenses/by/4.0/>.

References

- Jayakrishnan, R., Raj, A., Varma, S.J.: Self-assembled methylammonium lead bromide thin films with blue photoluminescence. *Appl. Nanosci.* **11**, 2095–2102 (2021). <https://doi.org/10.1007/s13204-021-01933-1>
- Shanker, U., Hussain, C.M., Rani, M.: Green nanomaterials for industrial applications. Elsevier, Amsterdam (2022). <https://doi.org/10.1016/C2019-0-05237-5>
- Cui, Z., Korotcenkov, G.: Solution processed metal oxide thin films for electronic applications. Elsevier, Amsterdam (2022). <https://doi.org/10.1016/C2017-0-02104-3>
- Faisal, A.D., Khalef, W.K.: Morphology and structure of CuO nanostructures grown via thermal oxidation on glass, silicon, and quartz at different oxidation temperatures. *J. Mater. Sci. Mater. Electron.* **28**(24), 18903–18912 (2017). <https://doi.org/10.1007/s10854-017-7844-z>
- Kaur, J., Khanna, A., Kumar, R., Chandra, R.: Growth and characterization of Cu₂O and CuO thin films. *J. Mater. Sci. Mater. Electron.* **33**(20), 16154–16166 (2022). <https://doi.org/10.1007/s10854-022-08506-0>
- Abdel-Galil, A., Moussa, N.L., Yahia, I.S.: Study on spray deposited Ni-doped CuO nanostructured thin films: microstructural and optical behavior. *J. Mater. Sci. Mater. Electron.* **33**(8), 4984–4999 (2022). <https://doi.org/10.1007/s10854-021-07688-3>
- Jung, Y.S., Kim, K.H.: Effects of post-annealing treatment on the properties of reactive sputtered cuprous-oxide thin films. *J. Korean Phys. Soc.* **67**(6), 1013–1017 (2015). <https://doi.org/10.3938/jkps.67.1013>
- Raship, N.A., Sahdan, M.Z., Adriyanto, F., Nurfazliana, M.F., Bakri, A.S.: Effect of annealing temperature on the properties of copper oxide films prepared by dip coating technique. In: AIP Conference Proceedings, vol. 1788 (2017). <https://doi.org/10.1063/1.4968374>
- Yisau Fasasi, A.: Effect of precursor solvents on the optical properties of copper oxide thin films deposited using spray pyrolysis for optoelectronic applications. *Am. J. Mater. Synth. Process.* **3**(2), 12 (2018). <https://doi.org/10.11648/j.ajmsp.20180302.12>
- Momeni, M.M., Ghayeb, Y., Menati, M.: Facile and green synthesis of CuO nanoneedles with high photo catalytic activity. *J. Mater. Sci. Mater. Electron.* **27**(9), 9454–9460 (2016). <https://doi.org/10.1007/s10854-016-4992-5>
- Jayakrishnan, R., Anand, A.M., Nair, V.G.: Flexible CuO-ZnO nano-bulk junction with photovoltaic response. *Mater. Res. Express* **6**, 1250d9 (2020)

12. Ekthammathat, N., Thongtem, T., Thongtem, S.: Antimicrobial activities of CuO films deposited on Cu foils by solution chemistry. *Appl. Surf. Sci.* **277**, 211–217 (2013). <https://doi.org/10.1016/j.apsusc.2013.04.027>
13. Thangavel, S., Suganthi, N.: Light sensitivity and electrical properties of two-dimensional nanoleaf CuO/ITO thin films. *J. Mater. Sci. Mater. Electron.* **31**(14), 11967–11974 (2020). <https://doi.org/10.1007/s10854-020-03751-7>
14. Gnanasekar, T., et al.: Enhanced opto-electronic properties of X-doped (X = Al, Ga, and In) CuO thin films for photodetector applications. *J. Mater. Sci. Mater. Electron.* **33**(23), 18786–18797 (2022). <https://doi.org/10.1007/s10854-022-08728-2>
15. Wang, W., Liu, Z., Liu, Y., Xu, C., Zheng, C., Wang, G.: A simple wet-chemical synthesis and characterization of CuO nanorods. *Appl. Phys. A Mater. Sci. Process.* **76**(3), 417–420 (2003). <https://doi.org/10.1007/s00339-002-1514-5>
16. Irwin, J.C., Chrzanowski, J., We1, T., Lockwood, D.J., Wold, A.: Raman scattering from single crystals of cupric oxide (1990)
17. Lin, H.H., Wang, C.Y., Shih, H.C., Chen, J.M., te Hsieh, C.: Characterizing well-ordered CuO nanofibrils synthesized through gas-solid reactions. *J. Appl. Phys.* **95**(10), 5889–5895 (2004). <https://doi.org/10.1063/1.1690114>
18. Zhang, Q., et al.: CuO/Cu₂O nanowire arrays grafted by reduced graphene oxide: synthesis, characterization, and application in photocatalytic reduction of CO₂. *RSC Adv.* **7**(69), 43642–43647 (2017). <https://doi.org/10.1039/c7ra07310k>
19. Jana, S., Das, S., Das, N.S., Chattopadhyay, K.K.: CuO nanostructures on copper foil by a simple wet chemical route at room temperature. *Mater. Res. Bull.* **45**(6), 693–698 (2010). <https://doi.org/10.1016/j.materresbull.2010.02.014>
20. Shang, D., et al.: Magnetic and field emission properties of straw-like CuO nanostructures. *Appl. Surf. Sci.* **255**(7), 4093–4096 (2009). <https://doi.org/10.1016/j.apsusc.2008.10.103>
21. Yang, Q., Yan, P.X., Chang, J.B., Feng, J.J., Yue, G.H.: Growth of bicrystal CuO microsheets from aqueous solution. *Phys. Lett. Sect. A Gen. At. Solid State Phys.* **361**(6), 493–496 (2007). <https://doi.org/10.1016/j.physleta.2006.07.056>
22. Song, H.J., Seo, M.H., Choi, K.W., Jo, M.S., Yoo, J.Y., Yoon, J.B.: High-performance copper oxide visible-light photodetector via grain-structure model. *Sci. Rep.* (2019). <https://doi.org/10.1038/s41598-019-43667-9>
23. Jana, R., Sil, S., Dey, A., Datta, J., Ray, P.P.: Analysis of temperature dependent electrical performance of Al/CuO/ITO Schottky barrier diode and explanation of inhomogeneous barrier heights by double Gaussian distribution. *AIP Adv.* (2018). <https://doi.org/10.1063/1.5066258>
24. Sürücü, B., Güllü, H.H., Terlemezoglu, M., Yildiz, D.E., Parlak, M.: Determination of current transport characteristics in Au-Cu/CuO/n-Si Schottky diodes. *Physica B Condens. Matter* **570**, 246–253 (2019). <https://doi.org/10.1016/j.physb.2019.06.024>
25. Ot, H., Serin, T.: The electrical characterization of FTO/Ti/CuO diode fabricated by DC magnetron sputtering method. <https://ssrn.com/abstract=3980024>. Accessed 20 Sept 2023
26. Gayen, R.N., Paul, R., Biswas, S.: Schottky enabled enhanced UV detection by graphene oxide composited transparent ZnO thin films. *Appl. Surf. Sci.* (2020). <https://doi.org/10.1016/j.apsusc.2020.147149>
27. Venkateswari, P., Thirunavukkarasu, P., Ramamurthy, M., Balaji, M., Chandrasekaran, J.: Optimization and characterization of CuO thin films for P-N junction diode application by JNSP technique. *Optik (Stuttg)* **140**, 476–484 (2017). <https://doi.org/10.1016/j.ijleo.2017.04.039>
28. Yuan, B., Zheng, X.J., Chen, Y.Q., Yang, B., Zhang, T.: High photosensitivity and low dark current of photoconductive semiconductor switch based on ZnO single nanobelt. *Solid State Electron.* **55**(1), 49–53 (2011). <https://doi.org/10.1016/j.sse.2010.09.002>
29. Zhou, J., Chen, L., Wang, Y., He, Y., Pan, X., Xie, E.: An overview on emerging photoelectrochemical self-powered ultraviolet photodetectors. *Nanoscale* **8**(1), 50–73 (2016). <https://doi.org/10.1039/c5nr06167a>
30. Shikoh, A.S., Ahmad, Z., Touati, F., Shakoor, R.A., Bhadra, J., Al-Thani, N.J.: A BHJ-thin-film/liquid-electrolyte based electrochemical-sensor for visible light-detection. *RSC Adv.* **7**(56), 35445–35450 (2017). <https://doi.org/10.1039/c7ra06193e>
31. Costas, A., Florica, C., Preda, N., Kuncser, A., Enculescu, I.: Photodetecting properties of single CuO–ZnO core–shell nanowires with p–n radial heterojunction. *Sci. Rep.* (2020). <https://doi.org/10.1038/s41598-020-74963-4>
32. Jayakrishnan, R., Kurian, A.S., Nair, V.G., Joseph, M.R.: Effect of vacuum annealing on the photoconductivity of CuO thin films grown using sequential ionic layer adsorption reaction. *Mater. Chem. Phys.* **180**, 149–155 (2016)
33. Marathe, P., Khanna, S., Panieliya, S., Vanpariya, A.: Fabrication of copper oxide nanostructures for visible-light photodetector. In: *Materials Today: Proceedings*, pp. 129–133. Elsevier Ltd (2021). <https://doi.org/10.1016/j.matpr.2021.08.115>
34. Raveesh, S., Yadav, V.K.S., Paily, R.: CuO single-nanowire-based white-light photodetector. *IEEE Electron. Dev. Lett.* **42**(7), 1021–1024 (2021). <https://doi.org/10.1109/LED.2021.3081627>
35. Luo, L.B., et al.: One-dimensional CuO nanowire: synthesis, electrical, and optoelectronic devices application. *Nanoscale Res. Lett.* (2014). <https://doi.org/10.1186/1556-276X-9-637>
36. Raghavendra, P.V., Bhat, J.S., Deshpande, N.G.: Visible light sensitive cupric oxide metal-semiconductor-metal photodetectors. *Superlatt. Microstruct.* **113**, 754–760 (2018). <https://doi.org/10.1016/j.spmi.2017.12.014>
37. Tripathi, A., Dixit, T., Agrawal, J., Singh, V.: Bandgap engineering in CuO nanostructures: dual-band, broadband, and UV-C photodetectors. *Appl. Phys. Lett.* (2020). <https://doi.org/10.1063/1.5128494>
38. Lee, S., et al.: Sol-gel processed p-type CuO phototransistor for a near-infrared sensor. *IEEE Electron. Dev. Lett.* **39**(1), 47–50 (2018). <https://doi.org/10.1109/LED.2017.2779816>
39. Kajli, S.K., Ray, D., Roy, S.C.: Efficient UV–visible photodetector based on single CuO/Cu₂O core-shell nanowire. *J. Alloys Compd.* (2022). <https://doi.org/10.1016/j.jallcom.2021.162546>

Publisher's Note Springer Nature remains neutral with regard to jurisdictional claims in published maps and institutional affiliations.